metals

MDPI

Article

Experimental Investigation on the Effect of Pre-Deformation and Quenching Method on the Mechanical Properties of Aluminum Alloy 2219

Zhibiao Wang [1,*], Kekun Xu [2], Yahao Chen [2], Liwei Xie [2] and Zhuo Zhang [3,*]

[1] Science and Technology on Advanced High Temperature Structural Materials Laboratory, Beijing Institute of Aeronautical Materials, Beijing 100095, China
[2] State Key Laboratory of High-Performance Precision Manufacturing, Dalian University of Technology, Dalian 116024, China
[3] School of Energy and Power Engineering, Dalian University of Technology, Dalian 116024, China
* Correspondence: wangzhibiao07@126.com (Z.W.); zhuozhang@dlut.edu.cn (Z.Z.)

Abstract

This study investigated high-speed air-atomized water-mist impingement cooling of 2219 aluminum alloy plates using a self-developed spray-quenching setup. Cooling intensity was controlled by varying the water loading fraction, and cooling curves were recorded using embedded thermocouples. Solution–aging treatments with conventional water quenching and mist quenching were performed, and multi-pass pre-deformation routes were applied before and/or after solution treatment. Tensile properties were evaluated at room temperature. Mist impingement cooling achieved markedly higher cooling rates than air cooling, with peak values in the order of 10^3 °C/s. Higher cooling intensity improved quenching efficiency and increased strength after aging. Multi-pass pre-deformation enhanced yield strength, but reduced elongation at high deformation levels, revealing a strength–ductility trade-off. These results provide guidance for optimizing quenching and pre-deformation parameters in heat treatment of 2219 aluminum alloy components.

Keywords: 2219 aluminum alloy; multi-pass pre-stretching; spray cooling; solution aging treatment

1. Introduction

Aluminum alloy 2219 belongs to the Al–Cu–Mn series of aluminum alloys. Due to its high specific strength, excellent weldability, machinability, and heat-treatability, it has been widely applied in the aerospace field, particularly in rocket fuel tanks, supersonic aircraft structural components, and space station assemblies [1–3]. As a typical heat-treatable wrought aluminum alloy, heat treatment processes such as solution quenching and artificial aging are primary methods for enhancing its mechanical properties [4,5]. Quenching, a critical step in solution treatment, directly influences the composition and distribution of microstructures at room temperature through its cooling rate, thereby affecting a material's final mechanical properties [6–8]. However, 2219 aluminum alloy exhibits significant quenching sensitivity [9] due to the high diffusion rate of Cu atoms in the medium- to high temperature range, which readily leads to non-equilibrium precipitation during cooling. Achieving the desired mechanical properties necessitates sufficiently rapid cooling rates during quenching. Insufficient cooling rates can easily result in undesirable precipitation,

Check for updates

Academic Editor: Andrea Di Schino

Received: 17 December 2025
Revised: 6 February 2026
Accepted: 8 February 2026
Published: 16 February 2026

Copyright: © 2026 by the authors. Licensee MDPI, Basel, Switzerland. This article is an open access article distributed under the terms and conditions of the Creative Commons Attribution (CC BY) license.

uneven strengthening effects, and microstructural heterogeneity, ultimately degrading mechanical performance. For instance, Elgallad et al. [10] investigated the effect of cooling rates on precipitation kinetics in 2219 aluminum alloy castings using both air cooling and water quenching. The results indicated that compared to water quenching, the slower cooling rate during air quenching suppressed *O′*-phase precipitation while promoting *θ*-phase precipitation, ultimately causing deterioration in the mechanical properties of the 2219 aluminum alloy. Therefore, enhancing the quenching rate is crucial for refining the grain structure of 2219 aluminum alloy, improving its mechanical properties, and extending its service life.

Depending on how alloy components come into contact with water, the cooling process after solution treatment of aluminum alloys is typically categorized into immersion and spray-cooling methods [11]. Immersion cooling is one of the most widely adopted cooling methods in industrial heat treatment, commonly utilizing water or oil as coolants and offering a high cooling rate. However, the uncontrollable cooling rate of immersion cooling can easily lead to excessive temperature differences between the interior and exterior of a workpiece, creating significant temperature gradients. This induces substantial internal stresses, potentially causing workpiece cracking. Ma et al. [12] investigated the effect of quenching water temperature on the macro–micro performance of forged 2219 aluminum alloy rings. They found that at lower quenching temperatures, the overall mechanical properties of the forged rings deteriorated as water temperature increased. This degradation primarily resulted from excessively rapid cooling rates inducing substantial quenching residual stresses, which adversely affected the material's overall mechanical performance. Wang et al. [13] investigated the effect of cooling rate on the microstructure and mechanical properties of the nickel-based superalloy MAR-M247. Compared to immersion cooling, spray cooling, which generates multiphase fluids with high heat exchange by mixing gas and liquid, has emerged as a frontier research direction and core technological focus in heat treatment cooling due to its efficient and controllable heat-transfer characteristics [14,15]. Fan et al. [16] investigated the effect of asymmetric spray quenching on residual stresses in thick aluminum plates. They found that under symmetric spray-quenching conditions, residual stress magnitude decreased with reduced spray velocity. Additionally, the established finite element model accurately predicted the distribution of residual stresses after quenching.

In addition to the influence of quenching rate on the enhancement of mechanical properties, pre-stretching represents a critical strengthening approach for aluminum alloys. This process introduces a high density of dislocations into the microstructure through work hardening, which leads to an increase in strength accompanied by a reduction in ductility. Wang et al. [17] examined the influence of pre-deformation applied between solution treatment and aging on the mechanical behavior of 2219 aluminum alloy forgings. Their results demonstrated that relative to undeformed specimens, forgings subjected to 3% pre-deformation exhibited increases of 11.9% in tensile strength and 26.2% in yield strength, along with a pronounced reduction in forging anisotropy. He et al. [18] studied the effect of pre-compression deformation applied prior to solution treatment on the dissolution behavior of Al_2Cu second-phase particles in 2219 aluminum alloy. The authors reported a substantial reduction in both the area fraction and average size of coarse Al_2Cu particles as the level of pre-deformation increased. Moreover, the introduction of pre-deformation significantly improved the mechanical performance of the alloy, with yield strength showing particularly notable enhancement. Zheng et al. [19] investigated the effects of pre-compression deformation applied after quenching on residual stress evolution and microstructural characteristics in aluminum lithium alloys. Their findings revealed that the degree of residual stress relief initially increased and subsequently decreased as the

amount of pre-deformation rose. Concurrently, pre-compression deformation promoted competitive precipitation among the T1, θ', and δ' phases. Within a pre-deformation range of 3% to 5%, T1 precipitation was increasingly favored over θ', resulting in a continuous increase in T1-phase content and the eventual disappearance of the θ' phase. A comprehensive review of the literature indicates that current research and industrial applications of spray-quenching processes are largely concentrated on thick aluminum alloy plates, whereas high-speed air atomization water spray-cooling techniques for thin aluminum alloy plates have received comparatively limited attention. In addition, most existing studies on aluminum alloy heat treatment focus on the influence of thermal processing on macrostructural and microstructural evolution during a single deformation stage, such as either before or after solution treatment. Investigations addressing the combined or synergistic effects of pre-deformation applied both before and after solution treatment on the final mechanical properties of aluminum alloys remain scarce.

Therefore, the objective of this study was to systematically investigate the coupled effects of cooling intensity and pre-deformation route on the cooling behavior and mechanical properties of 2219 aluminum alloy. Specifically, (1) a self-developed spray-cooling experimental setup was employed to perform high-speed air-atomized water-mist impingement cooling on thin 2219 aluminum alloy specimens under multiple water loading fraction conditions, in order to evaluate the cooling efficiency, heat-transfer uniformity, and the underlying mechanisms; (2) solution–aging heat treatment experiments involving conventional water quenching and spray quenching with different water-mist ratios were conducted to examine their influence on mechanical properties; and (3) a systematically designed experimental matrix with different multi-pass pre-stretching levels applied before and/or after solution treatment was carried out to clarify the effects of pre-deformation on yield strength, ultimate tensile strength, and elongation. The results of this work are expected to provide experimental guidance for optimizing heat treatment processes of high-performance 2219 aluminum alloy components.

2. Materials and Methods

2.1. Aluminum Alloy Specimens

The test material used in this study was annealed 2219 GB standard cross-sectional uniaxial tensile aluminum alloy [20]. Its chemical composition is shown in Table 1. The primary alloying elements of this alloy include Cu, Mn, and Zr. Among these, Cu serves as the core element for forming the θ′ strengthening phase, while Mn and Zr help suppress recrystallization and refine grain size, thereby improving the material's microstructural uniformity and overall properties. All samples used in this study complied with GB/T 228.1-2010. Aluminum alloy plates were processed into standard tensile specimens using wire-cutting technology along the rolling direction. To minimize the influence of surface oxide films and surface defects on test results, all specimen surfaces were polished using 800-grit sandpaper.

Table 1. Chemical composition of 2219 aluminum alloy (wt.%).

Cu	Mn	Fe	Zr	Ti	Si	Zn	Mg	Al
6.52	0.35	0.21	0.17	0.05	0.05	0.02	0.01	92.62

2.2. Water-Mist Spray-Quenching Experiments

A schematic of the experimental setup is shown in Figure 1. The experimental system was developed based on established spray/mist impingement cooling principles reported in the literature [21], which utilize enhanced convective heat transfer and phase-change heat transfer during droplet impingement to achieve high and controllable cooling rates. It consisted of a water and an air delivery system that are both precisely regulated by the valves and flow meters. The main components of the system included a water pump, a centrifugal air blower, flow meters, valves, pressure gauges and temperature sensors, water recovery tank and data acquisition system. The furnace and transfer apparatus are omitted from Figure 1 for clarity.

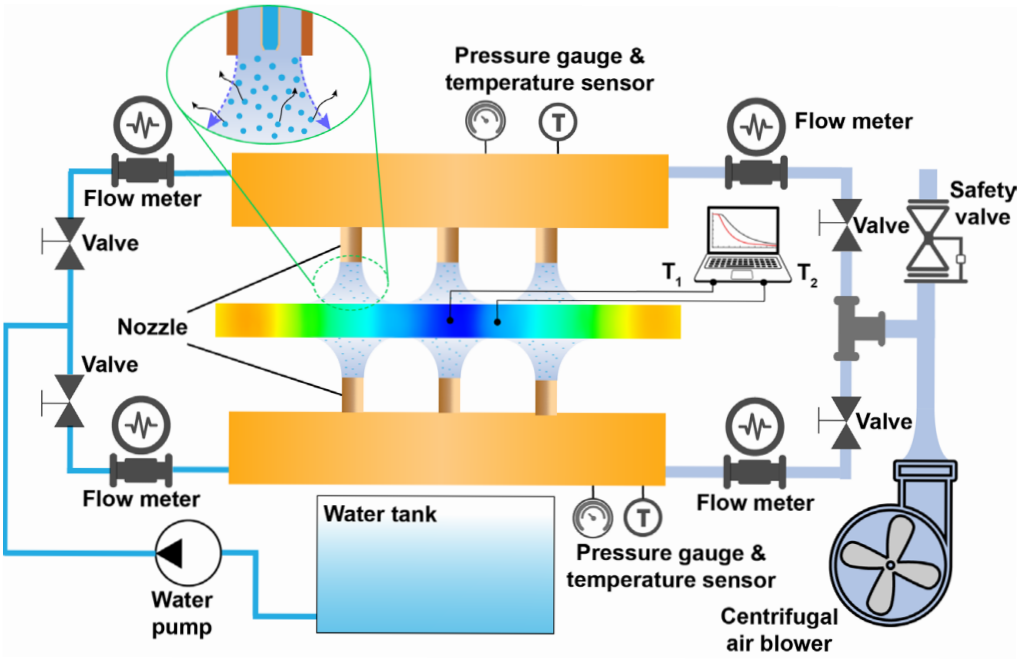


Figure 1. Schematic of the experimental system. The transfer apparatus, the furnace, and the intelligence system are not presented for better clarity.

The cooling platform consists of upper and lower cooling modules, as shown in Figure 2. The upper cooling platform is operated through a screw-driven lifting, and the lower platform is equipped with positioning blocks at each corner, ensuring precise alignment and firm installation of the cooling module. The geometrical details of the aluminum alloy 2219 workpiece are illustrated in Figure 2b. The workpiece was a square plate with dimensions of 50 mm × 50 mm × 4.5 mm (length × width × thickness). The workpiece temperature was measured using two type-K thermocouples (T1 and T2) embedded near the central region, with a horizontal offset of 7.5 mm from the outer boundary, as illustrated in Figure 2b. The thermocouple signals were recorded using a HIOKI temperature data logger with a sampling interval of 10 ms. The measured temperature–time data were used for subsequent cooling-rate analysis. A high-speed air-atomized water-mist spray (jet velocity > 100 m/s) with different water loading fractions was applied to quench the specimen, enabling controllable cooling rates. As shown in Figure 3, different water loading fractions were used to control the cooling rate of the solid solution quenching, followed by the same aging treatment procedure [22]. The detailed experimental plans are shown in Table 2.

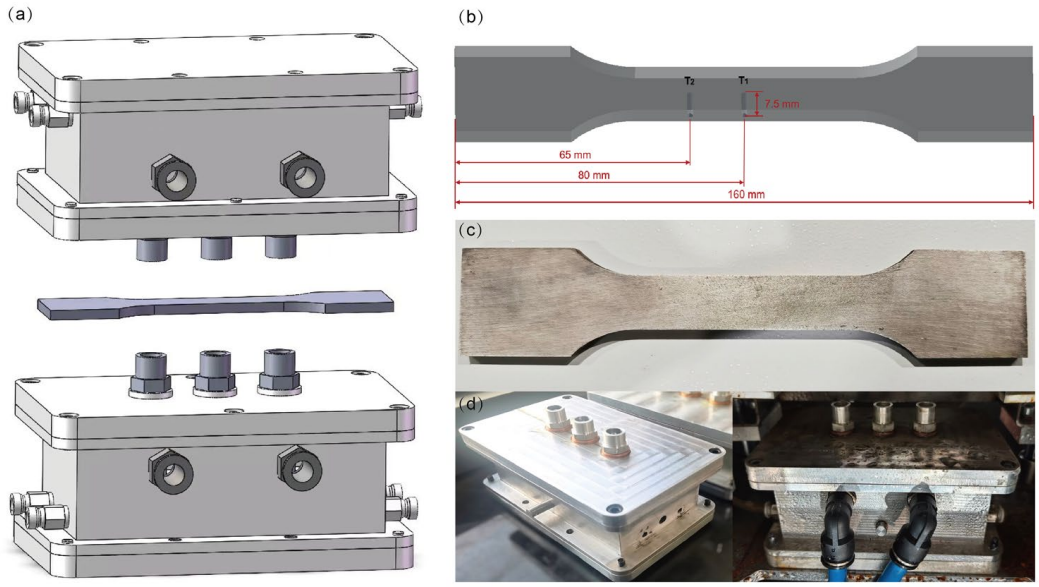


Figure 2. Cooling platform and workpiece. (**a**) 3D top and bottom cooling assembly with the workpiece in the middle; (**b**) dimensions and temperature sensor location; (**c**) photograph of the work piece; (**d**) photograph of the upper cooling platform (left). The cooling platform connected with the working media piping.

The instantaneous cooling rate was obtained from the measured temperature–time data by numerical differentiation using a finite-difference scheme. The cooling rate at time step i was calculated using Formula (1):

$$\dot{T}_i = -\frac{T_{i+1}-T_i}{\Delta t} \quad (1)$$

where T_i and T_{i+1} are the recorded temperatures at two consecutive sampling points and Δt is the sampling interval. In this study, $\Delta t = 10$ ms.

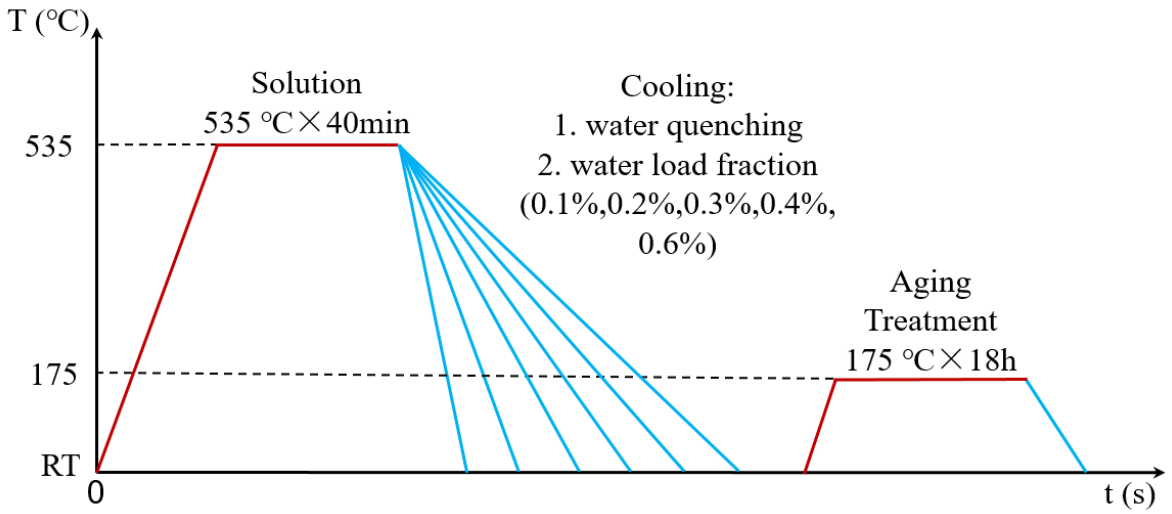


Figure 3. Schematic diagram of water-mist spray-quenching experiments. Red lines represent the heating stage, and blue lines represent the cooling/quenching stage.

Table 2. Experimental parameters for water-mist spray-quenching experiments. The water loading fraction is defined as $\phi = \dot{q}_w / (\dot{q}_w + \dot{q}_a)$, where $\dot{q}_w$ is the volumetric flow rate of water and $\dot{q}_a$ is the volumetric flow rate of air.

	O-State Pre-Stretching	Solution Treatment	Cooling Method	W-State Pre-Stretching	Aging Treatment
1	0	535 °C × 40 min	Water quenching	0	175 °C × 18 h
2			Spray cooling (ϕ = 0.10%)		
3			Spray cooling (ϕ = 0.20%)		
4			Spray cooling (ϕ = 0.30%)		
5			Spray cooling (ϕ = 0.40%)		
6			Spray cooling (ϕ = 0.60%)		

2.3. Heat Treatment Under Different Pre-Deformations

To investigate the influence of different pre-stretching deformations before and after solution treatment on the mechanical property of 2219 aluminum alloy, a series of heat treatment experiments was conducted following the procedure shown in Figure 4. The specimen dimensions used in this experiment were identical to those of the water-mist spray-quenching experimental specimens (50 mm × 50 mm × 4.5 mm). Prior to solution treatment, specimens were subjected to quasi-static tensile deformation at a strain rate of 0.001/s using a room-temperature tensile testing machine. The pre-stretching deformations were set to 0, 0.1, 0.2, and 0.25. The specimens were then solution-treated at 535 °C for 40 min to ensure complete dissolution of alloying elements. Rapid water quenching cooled them to room temperature, followed by secondary pre-deformation stretching with deformation levels of 0, 0.05, and 0.1. Subsequently, specimens underwent artificial aging at 175 °C for 18 h before air cooling to room temperature. All heat treatment parameters are detailed in Table 3.

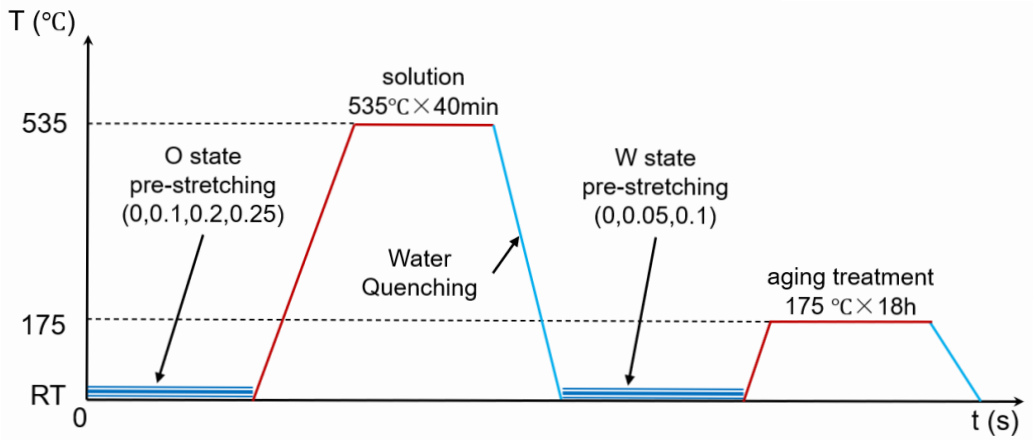


Figure 4. Schematic diagram of pre-strain heat treatment at different deformation levels. Red lines represent the heating stage, and blue lines represent the cooling/quenching stage.

Table 3. Experimental parameters under pre-deformations at different deformation levels.

	O-State Pre-Stretching	Solution Treatment	Cooling Method	W-State Pre-Stretching	Aging Treatment
1	0	535 °C × 40 min	Water quenching	0	175 °C × 18 h
2	0.1			0	
3	0.2			0	
4	0.25			0	
5	0.1			0.05	
6	0.2			0.05	
7	0.25			0.05	
8	0.1			0.1	
9	0.2			0.1	
10	0.25			0.1	
11	0			0	
12	0			0.05	
13	0			0.1	

2.4. Mechanical Testing

Room-temperature tensile tests were performed using a LE5105 computer-controlled electronic universal testing machine It was sourced from Lishi (Shanghai) Instruments Co., Ltd, located in Jinshan District, Shanghai, China. The tensile specimens followed the standard GB/T 228.1–2010, and the strain rate was set to 0.001 s^{-1}. Electron backscatter diffraction (EBSD) characterization was performed using a field-emission scanning electron microscope (FE-SEM, JSM-IT800, JEOL, Japan) equipped with an EBSD detector. Prior to EBSD analysis, the specimens were mechanically ground and subsequently electropolished to obtain a deformation-free surface suitable for orientation mapping. The EBSD data were acquired to analyze the geometrically necessary dislocation (GND) density and grain orientation spread (GOS), which were used to evaluate the dislocation structures and intragranular strain heterogeneity induced by different pre-deformation conditions.

For each processing condition, tensile tests were repeated five times (n = 5) to ensure repeatability. The reported mechanical properties represent the average values of the repeated measurements. For consistency and clarity, the mechanical property values reported in this manuscript are rounded to the nearest integer unless otherwise stated.

3. Results

3.1. Water Spray-Quenching Results

In Figure 5b, the instantaneous cooling rate and the average cooling rate are presented for the three jet composition configurations. The instantaneous cooling rate was calculated as the numerical derivative of the recorded temperature–time data using a finite-difference method with a sampling interval of Δt = 10 ms. The average cooling rate was calculated for temperature cooling from 450 °C to 300 °C, neglecting the cooling during the loading process. The x-axis is the temperature of the workpiece, and the y-axis is the corresponding cooling rate. A pure water jet experiment was also conducted for comparison. In the pure water jet, the water mass flow rate is the same as the water in the $\phi = 0.15\%$ scenario, corresponding to a jet velocity of U_0 = 4.86 m/s. The average cooling rate for water-mist cooling reaches 233.58 °C/s ($\phi = 0.15\%$) compared with that of dry air impingement 48.56 °C/s, revealing significant improvement on the performance in the terms of the

average cooling rate attributed to the effective cooling from phase change of the water droplet. With water cooling, the average cooling rate is 118.25 °C/s between the dry air and water mist. The instant cooling rate, defined as the time derivative of the surface temperature, is illustrated in Figure 5b. The peak cooling rate $\dot{T}_{max}$ for $\phi = 0.15\%$ water mist reaches 1760 °C/s, significantly exceeding those using dry air ($\dot{T}_{max} = 120$ °C/s) and pure water ($\dot{T}_{max} = 698$ °C/s).

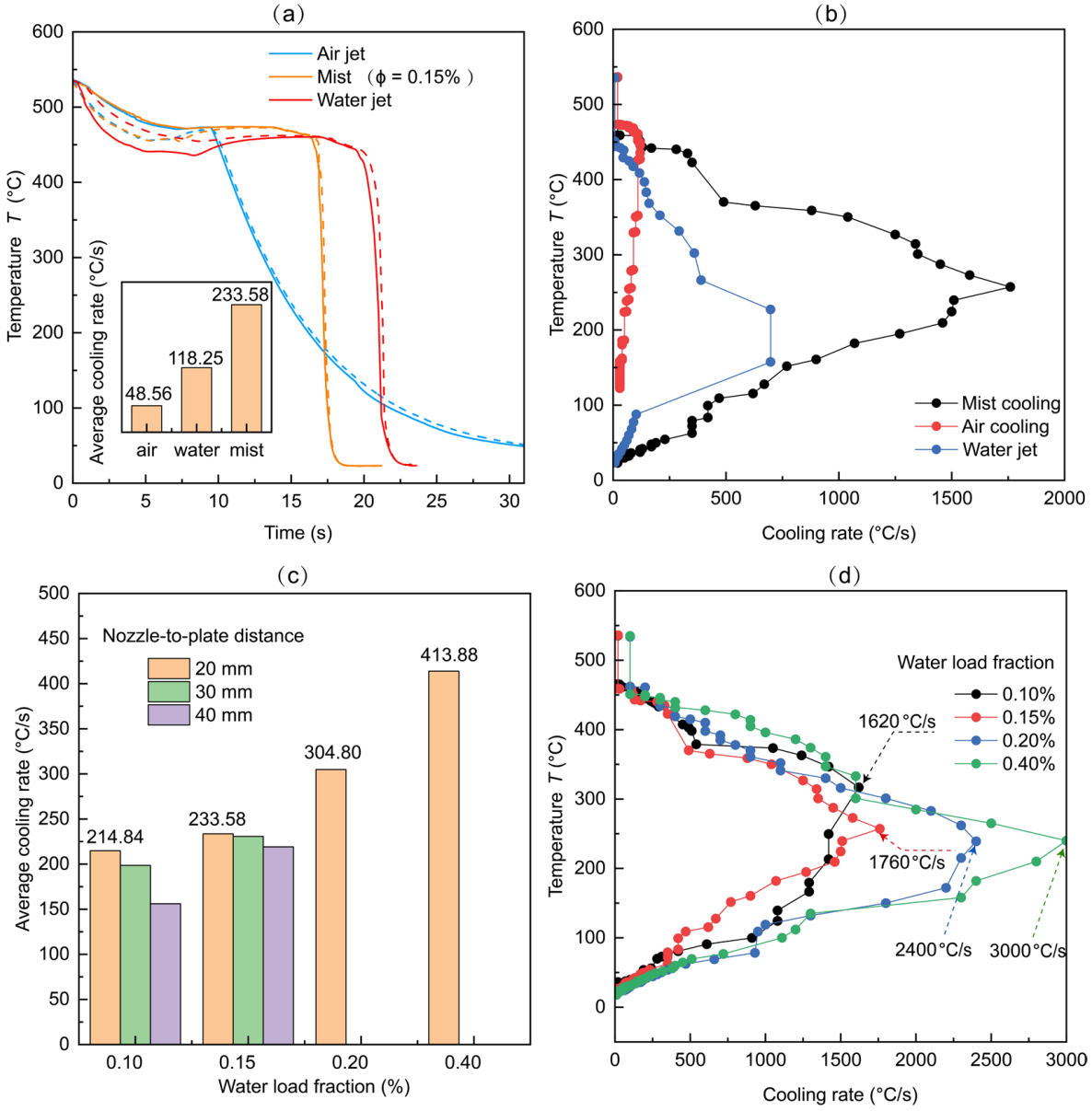


Figure 5. Temperature profile and cooling rate (**a**) T_1 (solid line) and T_2 (dashed line) evolution under different cooling media: air jet (U_0 = 110 m/s), mist (U_0 = 110 m/s, $\phi = 0.15\%$), water jet (U_0 = 4.86 m/s); (**b**) instantaneous cooling rate for different cooling media; (**c**) average cooling rate for different ϕ and nozzle-to-plate distance; (**d**) instantaneous cooling rate for different ϕ. The values shown represent average results from three repeated tests.

The mist jet initiates rapid heat removal almost immediately after impingement, as evidenced by the high cooling rate discussed above, attributable to the high surface area-to-volume ratio of microdroplets and the intense boiling upon contact with the hot surface. In addition, the micro-droplet accelerated by the high-speed air flow in the air-atomized water mist has enough momentum to rupture the vapor layer and achieve effective cooling

via phase change. Finally, the airflow can also facilitate in rapidly removing the generated vapor, thereby suppressing vapor accumulation. In contrast, the pure water jet forms a continuous liquid film on the surface, which initially delays efficient heat transfer until nucleate boiling is established. The air jet, due to the inherently low heat capacity of air and absence of a phase-change mechanism, relies solely on convective cooling, which is less effective, resulting in limited overall cooling performance. The extremely high peak cooling rates (above 10^3 °C/s) are mainly attributable to the combined effects of (i) the very large surface area-to-volume ratio of the microdroplets, (ii) intense phase-change heat transfer during droplet impingement and evaporation, and (iii) the high-speed airflow, which enhances convective heat removal and helps disrupt the vapor layer near the hot surface. Therefore, the measured peak cooling rates of 1000–3000 °C/s are physically reasonable for high-speed air-atomized mist impingement cooling [15,23].

Figure 5c illustrates the average cooling rate, while Figure 5d shows the instantaneous cooling rate with water load fraction ranging from 0.1% to 0.4%. As seen in Figure 5c, for $\phi = 0.1\%$, increasing nozzle-to-plate distance H from 20 mm to 40 mm leads to a 27% reduction in the average cooling rate. As the water load fraction increases, the effect of H in the present study becomes less pronounced, for example, at $\phi = 0.15\%$, only a 6.2% reduction is observed. This is mainly because a larger H normally increases the evaporation ratio, thereby reducing the mass of liquid-phase droplets reaching the target surface and weakening micro-droplet evaporative cooling. Increasing ϕ enhances the surface wetting and droplet coverage, which mitigates the sensitivity of cooling performance to H. It is observed that as the water load fraction increases, the average cooling rate also increases, reaching 413.88 °C/s for $\phi = 0.4\%$.

The instantaneous cooling rate for varying ϕ is presented in Figure 5d. It reveals that the instantaneous cooling rate increases with increasing ϕ, with a maximum cooling rate $\dot{T}_{\max} = 3000$ °C/s for $\phi = 0.4\%$ compared with $\dot{T}_{\max} = 1620$ °C/s for $\phi = 0.1\%$, yielding an almost 50% improvement. The maximum water load fraction $\phi = 0.4\%$ utilized in the present study is restricted by the current system, as the hydraulic resistance of the water flow path limits the pump delivery capacity. Although a higher water load fraction might enhance cooling capacity, it should not become excessively high to avoid locally liquid film accumulation. Under excessively high water load fractions, the dense droplets tend to agglomerate upon impingement, leading to reduced effective contact area and diminished single-droplet kinetic energy, which weakens the droplet–surface impact intensity and reduces the capacity to disrupt the vapor layer. In addition, excessive droplets can induce flow blockage near the surface, causing boundary-layer distortion and deteriorating the uniformity of the surface temperature, thus enlarging the spatial gradient of the cooling rate and degrading quench uniformity. Moreover, large droplets may deflect the mainstream flow, disturb the shear-layer structure near the surface, and trigger unexpected recirculation zones, complicating spray-field control.

The cooling rate variation curves for the entire process and the quenching-sensitive zone under different conditions are shown in Figure 6. These curves illustrate the changes in cooling rate under varying water load fraction. It can be observed that both the overall cooling process and the cooling within the quenching-sensitive zone demonstrate increased cooling rates with higher water load fraction. The cooling rate reaches its maximum at $\phi = 0.40\%$, after which it begins to decrease as the ratio increases further. As the cooling rate increases, non-equilibrium precipitation during cooling can be more effectively suppressed, which is beneficial for maintaining a supersaturated solid solution and improving the subsequent aging response. Within the quenching-sensitive zone, varying water loading fractions influence cooling rates, thereby determining whether the alloy undergoes complete quenching. By analyzing these cooling rate variation curves, spray-cooling

parameters can be adjusted to precisely control phase transformations and optimize the alloy's final properties. Similar trends of enhanced cooling efficiency with increasing spray intensity have been reported in previous spray-cooling and mist-quenching studies [24–28]; however, the peak cooling rates achieved in the present work are higher, which can be attributed to the combined effect of high-speed airflow, fine-droplet atomization, and reduced workpiece thickness.

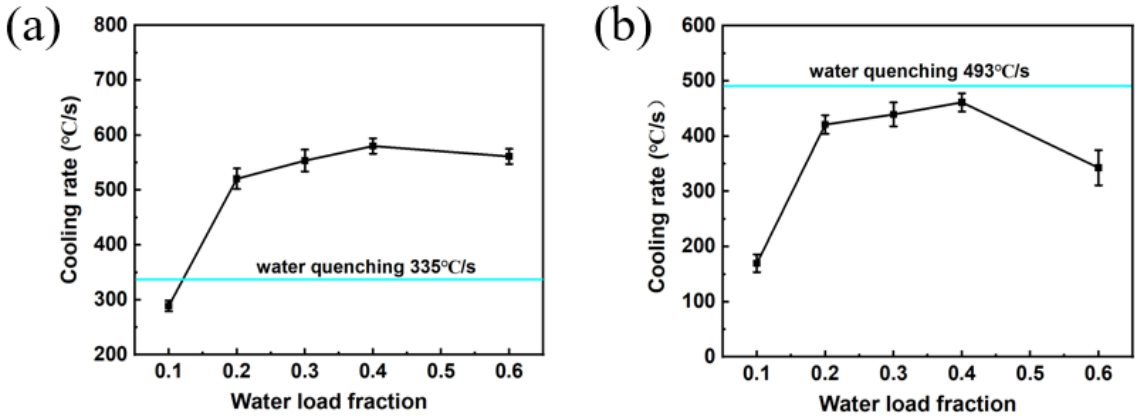


Figure 6. Heat treatment experiments under different cooling methods: (**a**) cold-hardening rate curve throughout the entire process under different conditions; (**b**) cold-shrinkage rate variation curves of quenching-sensitive zones under different conditions.

Specimens that underwent the entire heat treatment process were placed in a universal testing machine for room-temperature tensile testing. The engineering stress–strain curves obtained under different water loading fractions are shown Figure 7 below. At least three sets of tests were conducted for each condition, with the transfer time during spray quenching recorded for each. Except for isolated cases, the experimental data were reproducible, indicating that the variations were attributable to experimental random errors.

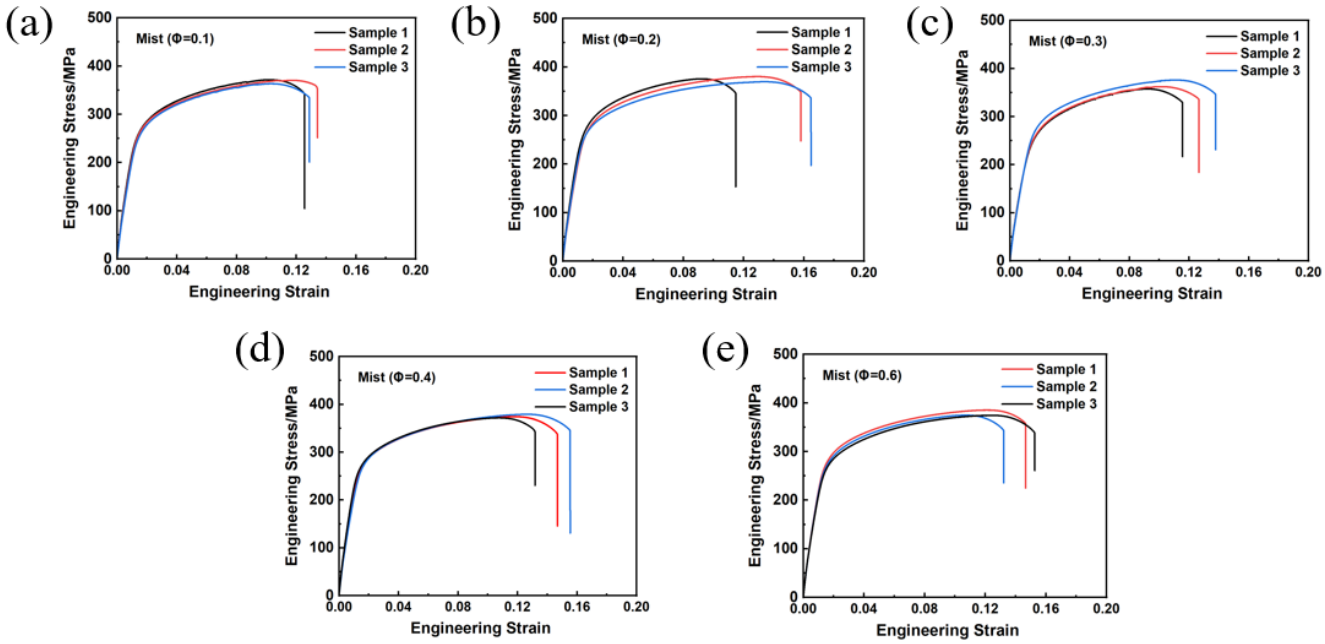


Figure 7. Tensile test at room temperature of the samples after heat treatment: (**a**) mist ($\phi = 0.10\%$); (**b**) mist ($\phi = 0.20\%$); (**c**) mist ($\phi = 0.30\%$); (**d**) mist ($\phi = 0.40\%$); (**e**) mist ($\phi = 0.60\%$).

Analysis curves reveal the mechanical properties of the material under different water loading fraction ratios, including yield strength, tensile strength, and elongation variation curves, as shown in Figure 8. The yield strength and tensile strength under different water loading fractions showed little variation, likely due to similar cooling processes. The maximum strength values occurred at $\phi = 0.40\%$ and $\phi = 0.60\%$, but both remained below the standard. This discrepancy may stem from prolonged transfer times causing slow room-temperature cooling coupled with a smaller contact area—and thus heat exchange area—between the water mist and the specimens compared to the standard.

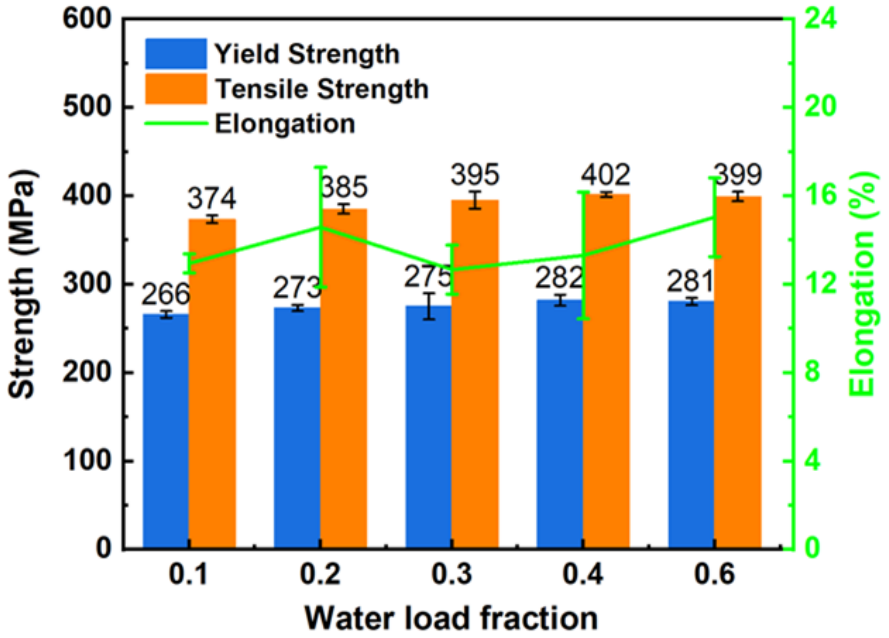


Figure 8. Comparison of material mechanical properties at different water loading fractions.

Although a higher cooling rate is generally beneficial for suppressing non-equilibrium precipitation during quenching and improving the subsequent aging response, excessively high cooling intensity may also induce large thermal gradients, which can increase quench-induced residual stress and the risk of distortion or cracking. Therefore, the optimization objective in practical heat treatment should not only focus on maximizing strength, but also consider maintaining sufficient ductility and minimizing residual stress and deformation.

Compared with conventional immersion quenching, the proposed air-atomized mist impingement cooling provides a more controllable cooling capacity. By adjusting key parameters such as the water loading fraction, nozzle-to-plate distance, and flow uniformity, the cooling rate and spatial temperature uniformity can be tailored to achieve a balanced combination of mechanical performance and quench quality.

Figure 9 present the SEM fractography of tensile fracture surfaces of 2219 aluminum alloy after T6 heat treatment under different water loading fractions. All specimens exhibit typical ductile fracture characteristics dominated by microvoid coalescence, indicating that plastic deformation remains the primary fracture mechanism.

At lower water loading fractions (0.1–0.2%), the fracture surfaces are characterized by deep and uniformly distributed dimples, suggesting sufficient plastic deformation prior to fracture. As the water loading fraction increases to 0.3–0.4%, the dimples become finer and less uniform, reflecting enhanced strengthening and reduced plastic deformation capacity.

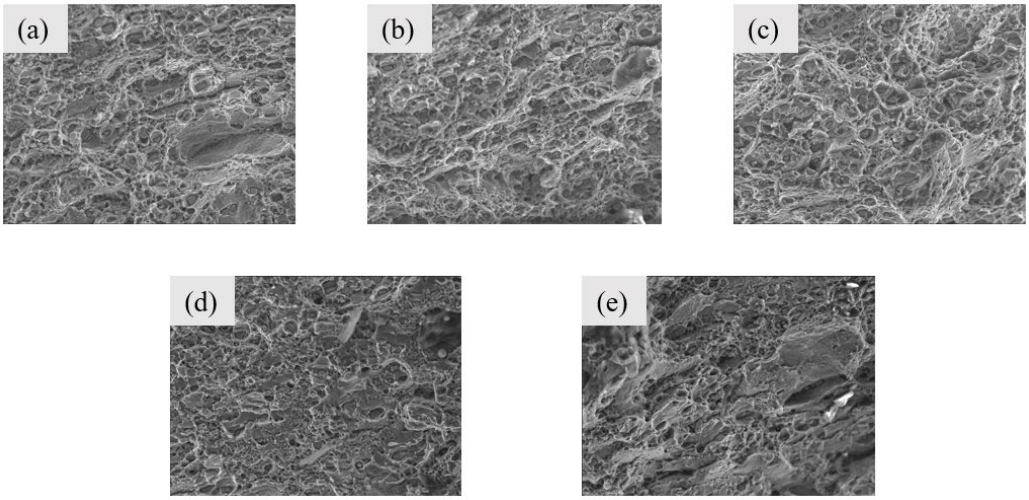


Figure 9. Fracture morphology of room-temperature tensile specimens under different water vapor ratios: (**a**) mist ($\phi = 0.10\%$); (**b**) mist ($\phi = 0.20\%$); (**c**) mist ($\phi = 0.30\%$); (**d**) mist ($\phi = 0.40\%$); (**e**) mist ($\phi = 0.60\%$).

At the highest water loading fraction (0.6%), the fracture surfaces show noticeably shallower dimples and locally flattened regions, indicating restricted microvoid growth and coalescence. This transition in fracture morphology is consistent with the observed decrease in elongation and can be attributed to the combined effects of higher cooling rates, increased dislocation density, and enhanced precipitation strengthening, which collectively limit dislocation mobility during tensile deformation.

3.2. Effect of Pre-Stretching in the O State

The experimental results are shown in Figure 10. Analysis revealed that the influence of O-state pre-deformation on the mechanical property of 2219 aluminum alloy exhibited distinct phase differences and quantitative effects. In the O state (initial pre-deformation state), as the pre-deformation amount increased from 0 to 0.25, the tensile strength rose from 156 MPa to 198 MPa, while yield strength surged from 65 MPa to 192 MPa. Pre-deformation directly strengthened the material by introducing dislocations and refining the microstructure. However, elongation decreased from approximately 35% to 10%, with plasticity markedly diminishing as deformation increased.

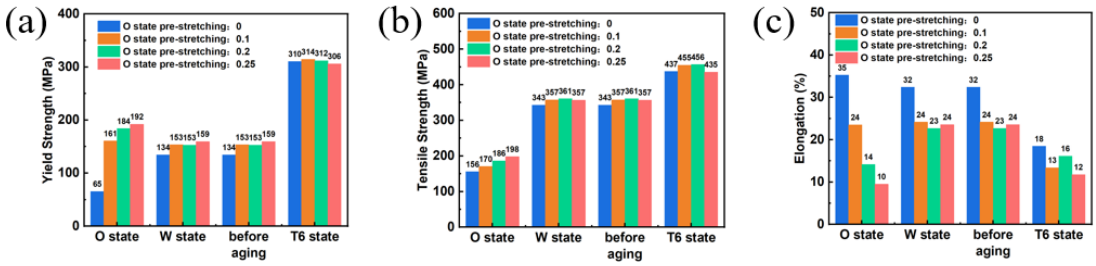


Figure 10. Tensile properties with no W-state pre-strain under different O-state pre-strain levels at room temperature of the samples after heat treatment: (**a**) yield strength; (**b**) tensile strength; (**c**) elongation.

Upon entering the W state (after solution treatment and water quenching), the strength differences caused by pre-deformation were partially offset. Tensile strengths across various pre-deformation levels clustered between 343 and 357 MPa, while yield strengths rose to 134–159 MPa. The recovery effect of solution treatment partially mitigated the microstructural distortion induced by pre-deformation, restoring elongation to 24–32%. Following

aging, material strength further increased substantially, with tensile strength reaching 437–456 MPa and yield strength at 306–314 MPa, with strength peaking at moderate pre-deformation levels (0.1–0.2). Excessive pre-deformation (0.25) caused a slight decrease in strength while further reducing elongation to 12–18%, with plasticity continuously declining as pre-deformation increased.

Overall, O-state pre-deformation serves as an effective strengthening method for 2219 aluminum alloy, significantly enhancing tensile and yield strengths across all stages while simultaneously sacrificing ductility. Moderate pre-deformation (0.1–0.2) represents the optimal range balancing strength and ductility. It promotes the dispersion precipitation of age-hardening phases through dislocation energy storage while avoiding microstructural inhomogeneity and excessive ductility reduction caused by excessive deformation.

To further clarify the role of pre-stretching in the O state in the present coupled processing route, EBSD-based geometrically necessary dislocation (GND) and grain orientation spread (GOS) analyses were conducted prior to solution treatment for samples subjected to different O-state pre-deformation levels. As shown in Figures 11 and 12, increasing O-state pre-deformation from 0 to 0.2 leads to a pronounced increase in dislocation density and intragranular orientation gradients.

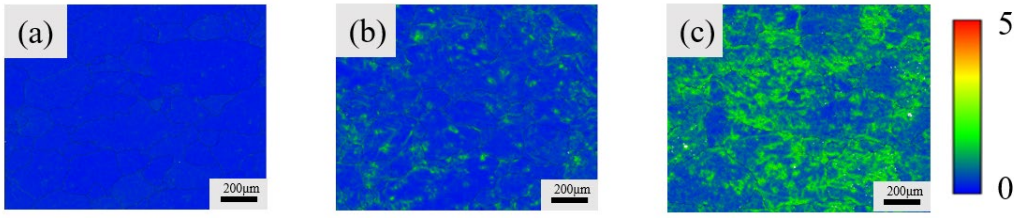


Figure 11. GND under different O-state pre-strains: (**a**) O-state pre-strain: 0; (**b**) O-state pre-strain: 0.1; (**c**) O-state pre-strain: 0.2.

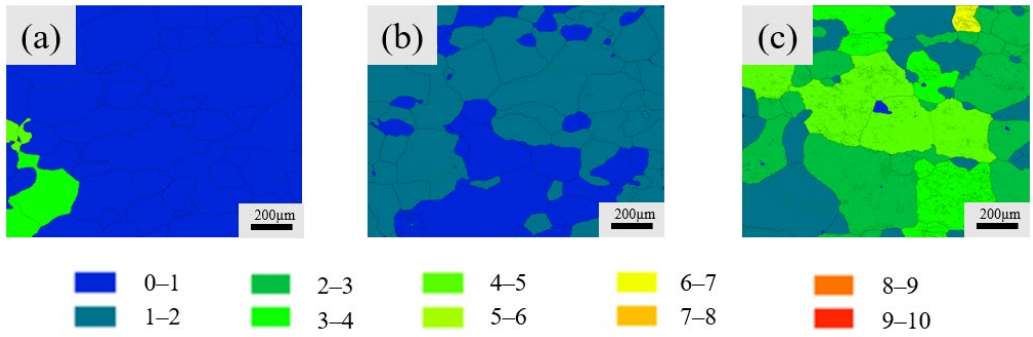


Figure 12. GOS under different O-state pre-strains: (**a**) O-state pre-strain: 0; (**b**) O-state pre-strain: 0.1; (**c**) O-state pre-strain: 0.2.

For the undeformed O-state sample, the GND density remains low and uniformly distributed, indicating a fully recrystallized and strain-free microstructure. With increasing pre-deformation, localized regions with elevated GND density and higher GOS values emerge, reflecting enhanced strain storage and lattice curvature. These dislocation structures are partially retained during subsequent solution treatment and act as preferential nucleation sites for precipitates during aging.

As a result, moderate O-state pre-deformation promotes strengthening through enhanced precipitation and dislocation–precipitate interactions, while excessive pre-deformation leads to pronounced strain heterogeneity and reduced ductility. When combined with controlled spray cooling, the synergistic effects of pre-deformation and cooling

rate govern the strength–ductility balance of the alloy, highlighting the unique contribution of the present processing strategy.

3.3. Effect of Pre-Stretching in the W-State

The experimental results are shown in Figure 13. The effect of pre-stretching deformation on the mechanical property of 2219 aluminum alloy exhibits a phased characteristic. During the O-state and W-state phases, pre-stretching had not yet been applied. Consequently, no differences were observed in tensile strength, yield strength, or elongation across varying deformation levels. The O state maintained its initial properties, while the W state demonstrated simultaneous enhancement due to solution treatment.

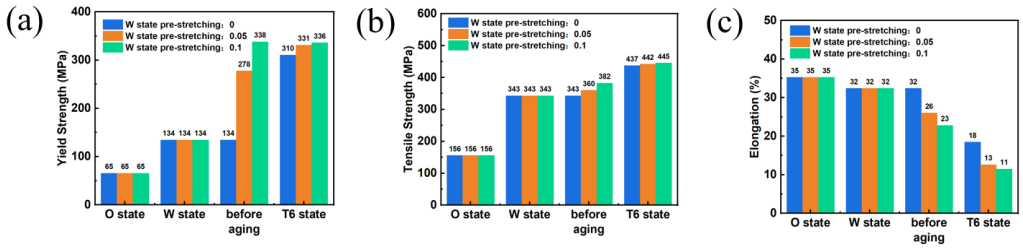


Figure 13. Tensile properties with no O-state pre-strain under different W-state pre-strain levels at room temperature of the samples after: (**a**) yield strength; (**b**) tensile strength; (**c**) elongation.

The strengthening effect of pre-stretching before aging becomes evident after deformation: as the pre-stretching deformation increases from 0 to 0.1, the tensile strength before aging rises from 343 MPa to 360 MPa, the yield strength jumps from 134 MPa to 338 MPa, and the elongation decreases to 23%. Post-aging properties further improved, with tensile strength reaching 437–445 MPa and yield strength reaching 310–336 MPa. Higher deformation rates correlated with greater strength, as the dislocations introduced by pre-stretching deformation directly strengthened the material while also providing more nucleation sites for strengthening phases during aging, achieving synergistic strengthening through deformation and aging.

However, increasing pre-stretch deformation simultaneously reduces material plasticity: post-aging elongation decreased from 18% to 12% as deformation increased from 0 to 0.1%. This results from dislocation entanglement and strengthening phases jointly hindering slip. Overall, however, pre-stretching deformation before aging proves an efficient strengthening method. A deformation of just 0.1 increases the post-aging yield strength by approximately 8%, achieving significant strength enhancement while maintaining plasticity within a reliable range.

To clarify the microstructural origin of the mechanical property variations, EBSD-based geometrically necessary dislocation (GND) density and grain orientation spread (GOS) analyses were performed for samples subjected to different W-state pre-deformation levels. As shown in Figures 14 and 15, increasing W-state pre-deformation from 0 to 0.1 leads to a pronounced increase in GND density and strain heterogeneity within the grains.

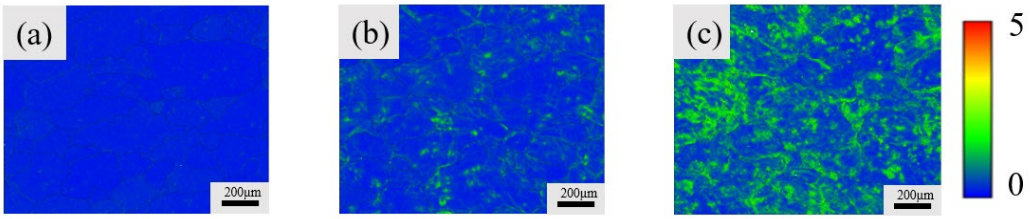


Figure 14. GND under different W-state pre-strains: (**a**) W-state pre-strain: 0; (**b**) W-state pre-strain: 0.0.05; (**c**) W-state pre-strain: 0.1.

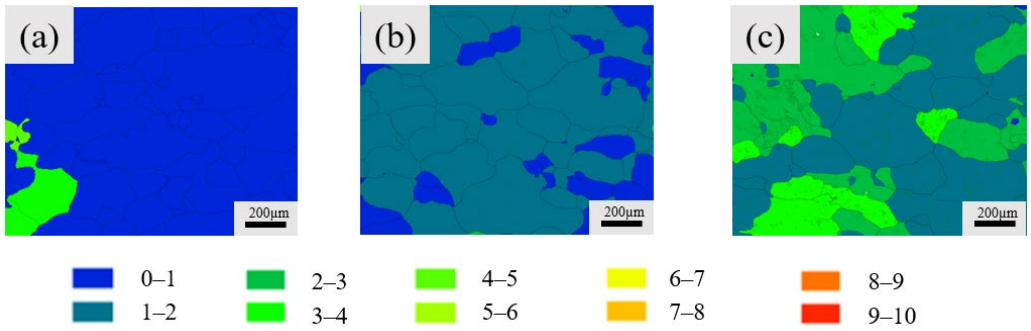


Figure 15. GOS under different W-state pre-strains: (**a**) W-state pre-strain: 0; (**b**) W-state pre-strain: 0.05; (**c**) W-state pre-strain: 0.1.

For the sample without pre-deformation, the GND density remains low and uniformly distributed, indicating limited strain accumulation after solution treatment. With increasing pre-deformation, localized regions with elevated GND density emerge, accompanied by higher GOS values, reflecting enhanced lattice curvature and intragranular misorientation. These dislocation structures act as effective obstacles to dislocation motion during subsequent tensile deformation, resulting in increased yield and tensile strength.

However, excessive pre-deformation introduces pronounced strain localization and heterogeneous dislocation distribution, which restricts plastic deformation coordination and accelerates damage initiation, leading to reduced ductility.

3.4. Effect of Coupled O-State Pre-Stretching and 0.05 Deformation in the W State

The experimental results are shown in Figure 16. The O-state pre-deformation and pre-aging deformation exhibited a pronounced coupled strengthening effect on the mechanical properties of the 2219 aluminum alloy. As the O-state pre-deformation increased from 0 to 0.25, the initial O-state tensile strength rose from 156 MPa to 198 MPa, with the W-state strength after solution treatment and water quenching also increasing synchronously. Following the superimposition of a secondary deformation of 0.05 before aging, dislocations accumulated further, providing more nucleation sites for strengthening phases during aging. Ultimately, the post-aging tensile strength reached 442–459 MPa and the yield strength reached 331–359 MPa, with peak strength observed at a pre-deformation of 0.1, demonstrating the synergistic strengthening effect of the dual-deformation process.

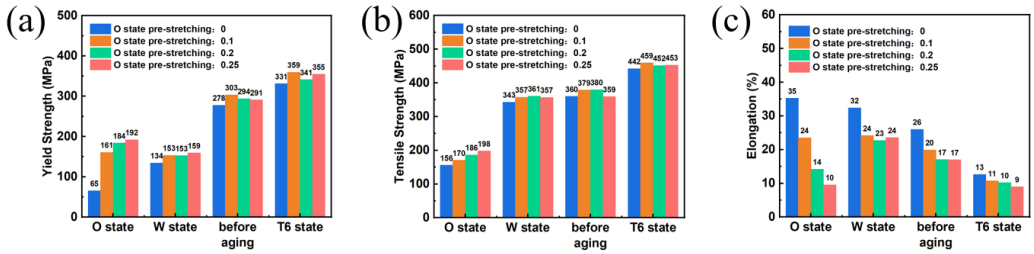


Figure 16. Tensile properties with W-state pre-strain of 0.05 under different O-state pre-strain levels at room temperature of the samples after heat treatment: (**a**) yield strength; (**b**) tensile strength; (**c**) elongation.

Concurrently, the coupled effect of these processes accelerated plasticity decay. As O-state pre-deformation increased from 0 to 0.25, elongation in the O state plummeted from 35% to 10%, and after superimposing secondary deformation before aging, the elongation further decreased to 7–26%. Ultimately, the elongation after aging remained only 8–13%. The greater the pre-deformation, the more pronounced the plasticity decline, which is because the dislocation entanglement introduced by pre-deformation and secondary

deformation, combined with the strengthening phases precipitated during aging, jointly hindered dislocation slip, leading to a continuous reduction in plasticity.

Overall, the optimal process combination balancing strength and ductility is an O-state pre-strain of 0.1 combined with a secondary strain of 0.05 before aging: under these parameters, the post-aging tensile strength reaches 459 MPa and the yield strength reaches 351 MPa, achieving maximum strength while maintaining elongation at 10%. This ensures plasticity remains within a reliable range despite significant strength enhancement, making it the ideal process parameter for the 2219 aluminum alloy under this processing route.

3.5. Effect of Coupled O-State Pre-Stretching and 0.1 Deformation in the W State

The experimental results are shown in Figure 17. For 2219 aluminum alloy, the O-state pre-deformation and pre-aging deformation exhibit a coupled effect of dual-deformation superposition strengthening. As the O-state pre-deformation increases from 0 to 0.1, the O-state tensile strength rises from 156 MPa to 170 MPa, while the strength of the solution-treated W state simultaneously increases to 357 MPa. Following secondary deformation of 0.1 before aging, the pre-aging tensile strength further increased to 395 MPa. After aging, the tensile and yield strengths ultimately reached 465 MPa and 357 MPa, respectively, both representing peak values. This occurs because the initial dislocations from O-state pre-deformation combine with newly generated dislocations from secondary deformation, providing more nucleation sites for the age-hardening phase, resulting in significant strengthening.

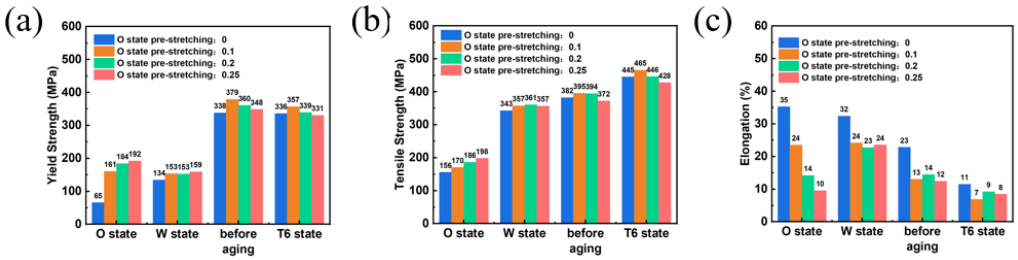


Figure 17. Tensile properties with W-state pre-strain of 0.10 under different O-state pre-strain levels at room temperature of the samples after heat treatment: (**a**) yield strength; (**b**) tensile strength; (**c**) elongation.

However, this coupling also accelerated plasticity decay. As the O-state pre-deformation increased from 0 to 0.25, the O-state elongation decreased from 35% to 10%, and after superimposing secondary deformation, the pre-aging elongation further decreased to 12%. Ultimately, the post-aging elongation ranged only between 7% and 12%. Greater pre-strain resulted in lower plasticity, attributable to the dual hindrance of dislocation entanglement and the aging-strengthening phase, causing the material's plasticity to continuously decrease with the accumulation of deformation.

Overall, a combination of 0.1% pre-strain in the O state and 0.1% strain before aging proves optimal. Under these parameters, post-aging strength reaches its peak (tensile 465 MPa, yield 357 MPa) while maintaining 9% elongation. This configuration maximizes strength while keeping plasticity within a reliable range, representing the ideal process parameters for achieving both high strength and plasticity in 2219 aluminum alloy under this processing route.

3.6. Correlation Between Processing Parameters and Mechanical Properties

Regarding the quenching condition, a higher cooling rate is expected to suppress non-equilibrium precipitation during cooling and retain more supersaturated solute in the matrix. This provides favorable conditions for subsequent precipitation during artificial

aging, which contributes to strength improvement. In contrast, insufficient cooling may promote premature precipitation during quenching, leading to reduced age-hardening potential and thus limiting the achievable mechanical performance.

Regarding the pre-deformation route, pre-stretching introduces a high density of dislocations into the alloy. These dislocations can directly contribute to strengthening through work hardening and can also serve as preferential nucleation sites for strengthening precipitates during aging, resulting in a coupled strengthening effect. However, excessive pre-deformation may lead to severe dislocation entanglement and localized strain accumulation, which reduces ductility and decreases elongation at fracture. Therefore, the strength–ductility trade-off observed in this work can be understood as the combined result of precipitation strengthening and dislocation strengthening under different cooling and pre-deformation conditions.

4. Discussion

Overall, the observed effects of cooling rate and pre-deformation on the mechanical properties of 2219 aluminum alloy are generally consistent with previous studies on spray quenching [24,25] and deformation-assisted aging of aluminum alloys [18,19], while the present work further highlights the influence of controllable mist impingement cooling and multi-pass deformation routes on the strength–ductility balance.

Similar enhancement of cooling efficiency with increasing spray intensity has been widely reported in spray or mist impingement cooling studies [26–28]. Cooling rates in the order of 10^3 °C/s have also been observed under intense spray-cooling conditions. Compared with some reported values, the relatively high peak cooling rates obtained in the present study can be attributed to the combined effects of high-speed airflow, fine droplet atomization, and the reduced thickness of the workpiece, which together facilitate rapid heat extraction.

From a process optimization perspective, the target should not only focus on maximizing strength, but also consider maintaining adequate ductility and reducing quench-induced residual stress and distortion. Compared with conventional immersion quenching in a standard T6 route, mist impingement cooling has the potential advantage of offering more controllable cooling capacity and improved cooling uniformity through parameter adjustment (e.g., water loading fraction and nozzle-to-plate distance). The multi-pass pre-deformation route can further enhance yield strength; however, excessive pre-deformation may lead to a pronounced reduction in elongation, highlighting the strength–ductility trade-off. Therefore, an optimized processing window should be determined by balancing cooling intensity and deformation level to achieve a desirable combination of strength and ductility.

The strengthening effect induced by pre-deformation observed in this study is in good agreement with previous reports on deformation-assisted aging of Al–Cu alloys [18,19], where increased dislocation density promotes precipitation strengthening during subsequent aging. At the same time, the reduction in elongation at higher pre-deformation levels reflects the typical strength–ductility trade-off widely reported in the literature. Differences in the extent of ductility loss among studies may result from variations in deformation level, deformation sequence, and heat treatment schedules.

Compared with single-stage pre-deformation, the present work introduces multi-pass pre-deformation routes applied at different processing states. This processing strategy leads to different deformation–aging interactions and thus results in mechanical responses that are not directly identical to those reported in the literature. The observed differences highlight the importance of deformation sequence and cooling history in tailoring the final properties of 2219 aluminum alloy.

It should be noted that the present study focused on the macroscopic mechanical response under different quenching and pre-deformation conditions. Although qualitative fractography analysis has been discussed based on SEM observations, a more quantitative characterization of fracture features (e.g., dimple size and distribution) will be conducted in future work to further correlate microstructural evolution with mechanical properties. Therefore, the discussion on ductility variation is mainly based on the observed tensile properties and established deformation/strengthening mechanisms. Detailed fracture surface characterization (e.g., SEM-based fractography) will be conducted in future work to further clarify the failure mechanisms under different processing conditions.

Although the current experimental setup is designed for laboratory-scale investigation, the proposed mist impingement cooling concept provides controllable cooling intensity and may be adapted for industrial applications after further simplification and scalability evaluation.

5. Conclusions

Based on a self-developed spray-cooling system, this study systematically conducted high-speed air-atomized water mist-cooling experiments under different water load fractions, providing an in-depth elucidation of the evolution of cooling efficiency and its underlying mechanisms as regulated by the water load parameter. On this basis, comparative heat treatment experiments involving water quenching and spray quenching with different water-mist ratios were further carried out using the same system to investigate the effects of different cooling methods on the macroscopic mechanical properties of the material. A systematic investigation of heat treatment processes incorporating multi-pass pre-deformation was performed, and the results indicated the following.

(1) Air-atomized mist achieves substantially higher average and instantaneous cooling rates compared with both air-jet and water-jet impingement cooling. Experiments demonstrated that at ϕ = 0.4%, the average cooling rate reaches 413.88 °C/s, significantly exceeding the values obtained with dry air (48.56 °C/s) and pure water (118.25 °C/s). As the water load fraction increases, both the maximum and average cooling rates rise, i.e., when ϕ increases from 0.1% to 0.4%, both values nearly doubled. Moreover, with higher ϕ, the sensitivity of the cooling performance to the nozzle-to-plate distance becomes notably reduced.

(2) In addition, during the spray-quenching experiments, within the quench-sensitive temperature range, an increase in the water vapor ratio leads to a higher cooling rate and an improvement in the macroscopic mechanical properties of the material.

(3) In the heat treatment experiments involving multi-pass pre-stretching, a combined process consisting of a pre-deformation of 0.1 applied before solution treatment and a pre-deformation of 0.1 applied after solution treatment enabled the material to achieve optimal mechanical performance after heat treatment. Compared with the reference specimens without pre-deformation, the yield strength increased by 12.4% and the tensile strength increased by 15.9%.

Limitations and future work

The present study mainly focused on the effects of quenching method/cooling rate and multi-pass pre-deformation routes on the macroscopic mechanical properties of 2219 aluminum alloy. In future work, systematic microstructural characterization (e.g., OM/SEM/TEM observation of precipitation features and EBSD analysis of grain morphology) will be performed to quantitatively establish the microstructure–property relationship. In addition, further optimization of spray parameters (water loading fraction

and nozzle-to-plate distance) will be conducted to achieve a balanced combination of high strength, adequate ductility, and reduced quench-induced residual stress and distortion.

In addition, it should be noted that excessively high cooling rates may increase thermal gradients and consequently enhance quench-induced residual stress and distortion risk. Therefore, future optimization should aim at achieving a balanced combination of high strength, adequate ductility, and reduced residual stress by tuning spray parameters (e.g., water loading fraction and nozzle distance) and improving cooling uniformity.

Therefore, the present results are generally consistent with existing literature trends, while the observed discrepancies emphasize the role of cooling method and deformation route in determining the mechanical behavior of 2219 aluminum alloy.

Author Contributions: Conceptualization, Z.Z. and Z.W.; methodology, Z.W. and L.X.; software, Z.W. and K.X.; validation, Y.C. and L.X.; formal analysis, Z.W. and L.X.; investigation, Z.W.; resources, Z.W.; data curation, Z.W.; writing—original draft preparation, Z.Z., Z.W., and K.X.; writing—review and editing, Z.Z. and Z.W.; visualization, Z.W. and Y.C.; supervision, Y.C.; project administration, Z.W.; funding acquisition, Z.W. All authors have read and agreed to the published version of the manuscript.

Funding: This work was supported by the financial support of AECC Innovation Program (CXPT-2024-010). And The APC was funded by CXPT-2024-010.

Informed Consent Statement: Not applicable.

Data Availability Statement: The original contributions presented in this study are included in the article. Further inquiries can be directed to the corresponding authors.

Conflicts of Interest: Author Zhibiao Wang was employed by the company Beijing Institute of Aeronautical Materials. The remaining authors declare that the research was conducted in the absence of any commercial or financial relationships that could be construed as a potential conflict of interest.

References

1. Song, H.; Gao, H.; Zhang, Q.; Zhou, X.; Zhang, B. Long-term stress relaxation behaviors and mechanisms of 2219 Al–Cu alloy under various temperatures and initial stresses. *J. Mater. Sci. Technol.* **2024**, *180*, 174–192. [CrossRef]
2. Guo, W.; He, H.; Yi, Y.; Huang, S.; Mao, X.; Fang, J.; Huang, J. Effects of axial cold-compression on microstructure uniformity and mechanical property enhancement of large 2219 Al–Cu alloy rings. *Mater. Sci. Eng. A* **2020**, *798*, 140233. [CrossRef]
3. Zhou, K.; Wang, J.; Feng, C.; Cheng, L.; Duan, Y.; Zhan, X. Stress distribution and evolution in 2219 aluminum alloy tank bottom structures during spinning and heat treatment. *Mater. Today Commun.* **2025**, *49*, 114001. [CrossRef]
4. Yang, J.; Ni, Y.; Li, H.; Fang, X.; Lu, B. Heat Treatment Optimization of 2219 Aluminum Alloy Fabricated by Wire-Arc Additive Manufacturing. *Coatings* **2023**, *13*, 610. [CrossRef]
5. Xie, B.; Huang, L.; Wang, Z.; Li, X.; Li, J. Microstructural evolution and mechanical properties of 2219 aluminum alloy from different aging treatments to subsequent electromagnetic forming. *Mater. Charact.* **2021**, *181*, 111470. [CrossRef]
6. Son, H.-W.; Lee, J.-M.; Cho, Y.-H.; Kim, S.-B. Effect of quench-rate on the mechanical property and nano-structure evolution of T6-treated Al-7Si-0.4 Mg casting alloy. *Mater. Charact.* **2025**, *229*, 115565. [CrossRef]
7. Fan, Z.; Lei, X.; Wang, L.; Yang, X.; Sanders, R. Influence of quenching rate and aging on bendability of AA6016 sheet. *Mater. Sci. Eng. A* **2018**, *730*, 317–327. [CrossRef]
8. Milkereit, B.; Fröck, H.; Schick, C.; Kessler, O. Continuous cooling precipitation diagram of cast aluminium alloy Al-7Si-0.3Mg. *Trans. Nonferrous Met. Soc. China* **2014**, *24*, 2025–2033. [CrossRef]
9. Wang, H.; Yi, Y.; Huang, S. Quench sensitivity of 2219 aluminum alloy. *Trans. Mater. Heat Treat.* **2016**, *37*, 67–72.
10. Elgallad, E.M.; Zhang, Z.; Chen, X.-G. Effect of quenching rate on precipitation kinetics in AA2219 DC cast alloy. *Phys. B Condens. Matter* **2017**, *514*, 70–77. [CrossRef]
11. Liu, H.; Hu, D.; Tao, X.; Li, J.; Qu, F.; Wang, S.; Li, X. Microstructure and mechanical properties of 2219-T6 aluminum thick plates processedby spray quenching. *J. Mater. Eng.* **2025**, *53*, 124–131.
12. Ma, Y.; Chen, S.; Wang, X.; Chen, K. Effect of Quenching Water Temperature on Microstructure and Mechanical Property of 2219 Aluminum Alloy Forging Ring. *J. Hunan Univ. (Nat. Sci.)* **2020**, *47*, 118–123.

13. Wang, Y.; He, J.; Hu, P.; Xiao, C.; Wang, X. Effect of Cooling Rate on the Microstructure and Mechanical Property of Nickel-Based Superalloy MAR-M247. *Materials* **2024**, *17*, 982. [CrossRef] [PubMed]
14. Liang, G.; Mudawar, I. Review of spray cooling—Part 1, Single-phase and nucleate boiling regimes, and critical heat flux. *Int. J. Heat Mass Transf.* **2017**, *115*, 1174–1205. [CrossRef]
15. Liang, G.; Mudawar, I. Review of spray cooling—Part 2, High temperature boiling regimes and quenching applications. *Int. J. Heat Mass Transf.* **2017**, *115*, 1206–1222. [CrossRef]
16. Fan, N.; Li, Z.; Li, Y.; Li, X.; Zhang, Y.; Xiong, B. Residual stress with asymmetric spray quenching for thick aluminum alloy plates. *Int. J. Miner. Metall. Mater.* **2023**, *30*, 2200–2211. [CrossRef]
17. Wang, H.; Yi, Y.; Huang, S. Influence of pre-deformation and subsequent ageing on the hardening behavior and microstructure of 2219 aluminum alloy forgings. *J. Alloys Compd.* **2016**, *685*, 941–948. [CrossRef]
18. He, H.; Yi, Y.; Huang, S.; Zhang, Y. Effects of cold predeformation on dissolution of second-phase Al2Cu particles during solution treatment of 2219 Al-Cu alloy forgings. *Mater. Charact.* **2018**, *135*, 18–24. [CrossRef]
19. Hou, H.; Zhang, L.; Xing, S.; Zhai, H.; Xia, S.; Zhai, L.; Wang, Z.; Liu, S. Effect of Pre-Deformation on the Microstructure and Precipitation Behavior of Spray-Formed 7xxx Series Aluminum Alloys. *Metals* **2025**, *15*, 365. [CrossRef]
20. *YS/T 1631-2023*; National Technical Committee on Standardization of Nonferrous Metals (SAC/TC 243). 2014 and 2219 Aluminum Alloy Forgings for Aerospace Applications. China National Institute of Metrology and Quality Inspection for Nonferrous Metals Industry: Beijing, China, 2023. (In Chinese)
21. Xu, R.; Zhang, R.; Jiang, J.; Wang, Z.; Zhang, Z.; Zheng, K.; Zhao, L. Investigation on the jet impingement cooling of steel discs using air-atomized water mist. *Int. J. Heat Mass Transf.* **2025**, *245*, 126989. [CrossRef]
22. Zheng, W.; Wang, S.; Yang, Q.; Yuan, W. Influence of precompression deformation on the residual stress, microstructure, and mechanical properties of aluminum–lithium alloys. *Mater. Charact.* **2025**, *220*, 114721. [CrossRef]
23. Wang, H.; Li, Y.; Wu, J. Effect of solution time on microstructure and mechanical properties of 2219 aluminum alloy. *Heat Treat. Met.* **2023**, *48*, 152–156.
24. Agrawal, C.; Lyons, O.F.; Kumar, R.; Gupta, A.; Murray, D.B. Rewetting of a hot horizontal surface through mist jet impingement cooling. *Int. J. Heat Mass Transf.* **2013**, *58*, 188–196. [CrossRef]
25. Guo, R.; Wu, J.; Liu, W.; Zhang, Z.; Wang, M.; Guo, S. Investigation of heat transfer on 2024 aluminum alloy thin sheets by water spray quenching. *Exp. Therm. Fluid Sci.* **2016**, *72*, 249–257. [CrossRef]
26. Ning, L.; Luo, S.; Li, Z.; He, L. Research on the heat transfer characteristics of air-atomized water spray cooling by experiment and inverse heat conduction method. *Heat Mass Transf.* **2022**, *58*, 1247–1262. [CrossRef]
27. Kita, Y.; Nakamatsu, M.; Hidaka, S.; Kohno, M.; Takata, Y. Quenching mechanism of spray cooling and the effect of system pressure. *Int. J. Heat Mass Transf.* **2022**, *190*, 122795. [CrossRef]
28. Wendelstorf, J.; Spitzer, K.; Wendelstorf, R. Spray water cooling heat transfer at high temperatures and liquid mass fluxes. *Int. J. Heat Mass Transf.* **2008**, *51*, 4902–4910. [CrossRef]

Disclaimer/Publisher's Note: The statements, opinions and data contained in all publications are solely those of the individual author(s) and contributor(s) and not of MDPI and/or the editor(s). MDPI and/or the editor(s) disclaim responsibility for any injury to people or property resulting from any ideas, methods, instructions or products referred to in the content.